Paper No. 170

Energy Harvesting based on the Hybridisation of two Smart Materials

Julian S. Gosliga[1], **Dr Olga A. Ganilova**[2]
[1,2]*Department of Mechanical Engineering, University of Sheffield*
Mappin Street, Sheffield, S1 3JD, UK

ABSTRACT

Recently, there has been an increased demand for power harvesting as a source of providing renewable energy. One of the most promising technologies due to their high power densities are piezoelectric devices, harvesting vibrational energy. There has been extensive research done in the area of energy harvesting using smart materials. However, the majority of this work is dedicated to the application of one type of smart material, such as piezoelectric or shape memory alloy. The aim of this paper is to develop a completely novel concept of a hybrid device combining piezoelectric and shape-memory alloy effects. The resulting device has a strong potential for miniaturisation and practical biomedical applications in environments characterised by thermal fluctuations. Both finite element and analytical models were developed to describe the dynamic behaviour of this innovative device. Both models predicted parametric behaviour for an input frequency of 988 Hz. Performance of the device was comparable to existing energy harvesting devices. The limitations and benefits of each modelling approach are also discussed.

[1] Research Scientist, jsgsoliga1@sheffield.ac.uk
[2] Lecturer, o.ganilova@sheffield.ac.uk

1 INTRODUCTION

Energy harvesting is a rapidly growing field that has gained much interest over recent years. One of the main reasons has been a desire to move away from reliance on batteries or external power sources. Various methods can be used to capture ambient energy from different sources and convert it into useful electrical energy, this opens up the possibility for self-powered devices. Energy harvesting devices have become more viable due to the growing development and applications of smart materials. Certain smart materials operate by converting one form of energy to another, making them well suited to harvesting energy. Piezoelectric materials possess some of the highest work densities, which makes them promising candidates for miniaturised generators. Vibrational energy harvesters use piezoelectric materials to convert kinetic energy to electrical energy. These are of interest for use in wireless condition monitoring, particularly in locations where there is a large amount of kinetic energy and the systems are isolated. The use of a secondary material effect could allow piezoelectric materials to be used for harvesting energy in new environments.

As stated previously, the possibility of using energy harvesting for powering remote devices is being explored. Their low power requirements and isolated nature means that wireless sensor networks, along with microelectromechanical (MEMS) systems, are key applications for energy harvesting technology [1]. Recently, there has been work investigating using energy harvesting to replace batteries in medical implants. Currently, changing the batteries powering a medical implant involves surgery, which limits the lifetime and applications of any implanted device [2].

Miniaturisation potential is seen as an important requirement when looking at energy harvesting methods in medical applications. Piezoelectric materials are considered promising smart materials for use in harvesters as the operation of a piezoelectric generator is well-understood. Furthermore, they possess high power densities, enabling even modestly sized harvesters to power attached circuitry [3]. Most of the time piezoelectric materials are used to

convert mechanical energy to electrical energy through the direct piezoelectric effect (DPE), with vibrational energy harvesters being the most common [4–6]. In addition, piezoelectric materials can convert fluctuating temperature to electrical energy via the pyroelectric effect [7]. The piezoelectric materials most frequently used in energy harvesting are piezoceramic lead zirconate titanate (PZT), the piezopolymer polyvinylidene flouride (PVDF) and epoxy-PZT macro-fibre composite (MFC) [8]. The two different coupling modes of piezoelectric materials can have a large effect on performance due to differences in the stiffness and the piezoelectric constant in each direction. Furthermore, the shape of the harvester can affect the efficiency of the device [9]. There have been several studies comparing different material and configuration choices generally, as well as for specific applications [10–12].

The shape memory effect (SME) is another smart material effect, which can be used for converting thermal energy to mechanical. The SME has not been widely explored for the purpose of energy harvesting and the mechanical energy is typically used to control vibration or to otherwise modify the shape and mechanical properties of a structure [13–17]. By embedding shape-memory alloy (SMA) wires into a matrix to form a composite, it is possible to control the stiffness and internal strain energy of the material. Researchers have been aware of SMAs for some time and as such comprehensive analytical and numerical (FE) models exist [18,19]. The efficiency of SMAs has been studied with recommendations for increasing the efficiency, along with a study of factors which affect other properties such as hysteresis and cycle time [20,21]. There is a wealth of information about how the composition and annealing techniques used to produce the SMA affect the properties [22].

Lately there have been some attempts to create a hybridisation of two or more smart materials for the purpose of energy harvesting. A hybrid device which combines the DPE, pyroelectric and SME would give an energy harvester with greater output than either a thermoelectric or pyroelectric generator of equivalent size [23]. Such a harvester would be easier to scale down than a thermoelectric generator. Additionally, it could be designed with a higher energy output per cycle than a pyroelectric generator, thus reducing the reliance on the frequency of temperature fluctuations. There have been attempts to combine SMA and piezoelectric on a centimeter scale and at a smaller scale, both experimentally and theoretically [24–26]. However, there has been little reasoning behind these attempts with regards to producing the best possible harvester. The experimental attempts largely fail to consider the theoretical aspects and vice versa. Hence an attempt to create an optimal hybrid harvesting solution for a specific application would be a significant contribution.

The aim of this work is to develop a model for a hybrid energy harvesting device (HEHD). The final device utilises both a shape memory and piezoelectric elements, though this paper focuses on the piezoelectric element. This paper describes the behaviour of the piezoelectric harvester and incorporates the SMA through the force applied. Both analytical and FE approaches have been used to model the device. The two approaches have been compared to verify the model and highlight the benefits and limitations of each approach.

The work of this paper is organised as follows. The next section describes the operation and application of the HEHD; the analytical model of the device; and the finite element (FE) model of the device. The third section examines the output of the models; verifies the analytical models against the FE model by looking at the displacement; and evaluates the output energy based on the displacement. This is followed by a discussion of the level of agreement between the two models; a comparison with existing energy harvesting methods; and recommendations for when the analytical or FE model is most appropriate.

2 MATERIALS AND METHODS

The models in this paper describe the dynamic behaviour of the piezoelectric composite plate, which generates electricity in the harvester. The effect of the SMA can be

incorporated through the forcing term. The FE model was produced using the commercial software package, ANSYS. In the FE model, the PZT material is represented by patches embedded into the carbon-fibre reinforced polymer (CFRP) host material. This is in contrast to the analytical models, which assume that the PZT is mixed homogenously with the CFRP in the two outer layers. However, the volume fraction for each model is kept the same. Representing the PZT material as patches should give a more realistic model, as in reality the PZT would be included as ceramic patches and not dispersed throughout the CFRP. By examining both cases, the difference that the PZT distribution has on the behaviour of the device can be seen. In addition, this provides the opportunity to explore different patch configurations using the PZT patch model.

2.1 Description of the hybrid energy harvesting device (HEHD)

The novel device being modelled is a hybridisation between the DPE and SME, using a contracting SMA element to bend two piezoelectric elements on either side, as shown in Fig. 1. This was chosen as it gives a simple and scalable thermal energy harvester. The device would ideally operate in an environment with large temperature fluctuations and a high heat transfer rate. Both of these factors would increase the activation speed of the SMA, thereby increasing the operating frequency and hence power. Such an environment could potentially be found within the human body [27], or factory and power-plant cooling ducts [28].

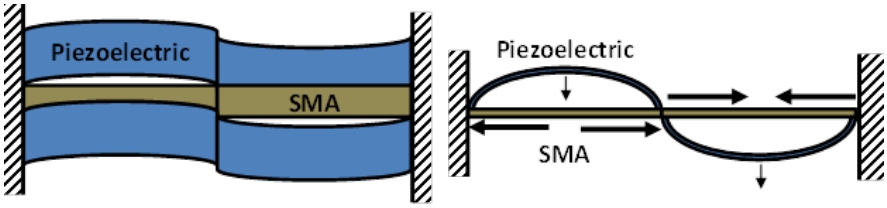

Figure 1. A schematic showing the full HEHD (arrows represent the device behaviour) during activation, as the SMA contracts the piezoelectric elements are deformed

2.2 Analytical approach

One of the ways to consider the problem is an analytical approach. In this case the SMA-composite and PZT-composite elements are represented by a slender sandwich plate with active layers (PZT or SMA composites) at the top and the bottom (Fig. 2), the composition of which can be altered and optimized according to [13,14].

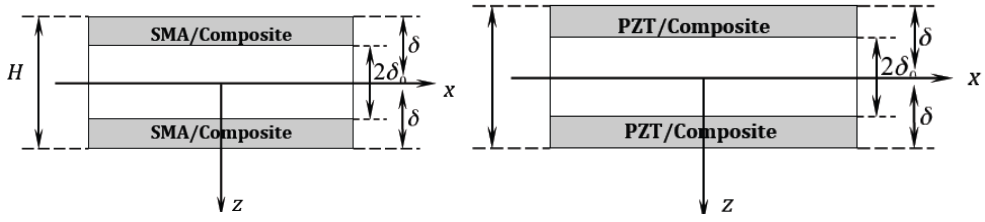

Figure 2. PZT and SMA-composite representation

Following the representation in [29] the piezoelectric elements are treated as anisotropic layers held at all four corners with negligible *z*-displacement.

Under a stress (σ) generated by the SMA composite, the voltage generated due to the direct piezoelectric effect is $\sigma g_{ij} t_p$, where g_{ij} is the piezoelectric voltage constant (electric field per unit stress), t_p is the piezoelectric layer thickness, and the stresses in *x* and *y* are [29]

$$\begin{aligned}\sigma_x &= \overline{Q_{11}}(\varepsilon_x^0 + zk_x) + \overline{Q_{12}}\left(\varepsilon_y^0 + zk_y\right) + \overline{Q_{16}}(\varepsilon_{xy}^0 + zk_{xy}) \\ \sigma_y &= \overline{Q_{12}}(\varepsilon_x^0 + zk_x) + \overline{Q_{22}}\left(\varepsilon_y^0 + zk_y\right) + \overline{Q_{26}}(\varepsilon_{xy}^0 + zk_{xy})\end{aligned} \tag{1}$$

where $\overline{Q_{ij}}$ are transformed stiffness terms which can be found for a transversely isotropic material from [30]:

$$\begin{aligned}\overline{Q_{11}} &= c^4Q_{11} + s^4Q_{22} + 2c^2s^2(Q_{12} + 2Q_{66}) \\ \overline{Q_{22}} &= s^4Q_{11} + c^4Q_{22} + 2c^2s^2(Q_{12} + 2Q_{66}) \\ \overline{Q_{12}} &= c^2s^2(Q_{11} + Q_{22} - 4Q_{66}) + (c^4 + s^4)Q_{12} \\ \overline{Q_{66}} &= c^2s^2(Q_{11} + Q_{22} - 2Q_{12}) + (c^2 - s^2)Q_{66} \\ \overline{Q_{16}} &= cs\left(c^2Q_{11} - s^2Q_{22} - [c^2 - s^2](Q_{12} + 2Q_{66})\right) \\ \overline{Q_{26}} &= cs\left(s^2Q_{11} - c^2Q_{22} + [c^2 - s^2](Q_{12} + 2Q_{66})\right)\end{aligned} \tag{2}$$

where $c = \cos\theta$; $s = \sin\theta$; θ is dependent on the stacking of plies; $[Q]$ is the stiffness matrix; and ε^0 are mid-plane strains of a PZT-component, which are small relative to the out-of-plane components, k_i, $(i = x, y, xy)$ are the laminate curvatures defined as

$$k_x = -\frac{\partial^2 w^0}{\partial x^2};\ k_y = -\frac{\partial^2 w^0}{\partial y^2};\ k_{xy} = -\frac{2\partial^2 w^0}{\partial x \partial y} \tag{3}$$

where w^0 is the out-of-plane displacement of the middle plane in the PZT-composite.

It should be emphasized that the structure in Fig. 1 is symmetrical with respect to coordinate *x* and *y*, therefore the out-of-plane displacement of a PZT element due to the compression of the SMA-composite is identical for both piezo-elements (in blue). Thus by identifying the displacement for one of the PZT-composite parts, it is possible to project the displacement for the other one. This means that in further discussion we will concentrate only on one PZT-composite, assuming that the behaviour of the other PZT-part is identical.

It should be pointed out that during compression, attached piezoelectric patches are strained in the poling direction 33 and transverse direction 31. Taking into account that the stress varies across the volume of piezoelectric patches, the electrical energy of piezo-elements for 0^o (top surface) and 90^o (bottom surface) is [29]

$$U = 4\sum_{m=1}^{2}\left[\frac{1}{2}\int_{v_1}\left(d_{33}g_{33}\sigma_x^2 + d_{31}g_{31}\sigma_y^2\right)dv_1 + \frac{1}{2}\int_{v_2}\left(d_{33}g_{33}\sigma_y^2 + d_{31}g_{31}\sigma_x^2\right)dv_2\right] \tag{4}$$

where coefficient 4 indicates two patches on the top surface of the PZT-element and two on the bottom, *m* defines the associated shape and v_1 and v_2 are the volumes of two layers on opposite laminate surfaces; the piezoelectric constants (charge per unit force) d_{ij} and g_{ij} are taken as the values found in Table 1.

Analysing the Eqs (1) – (4), it is possible to see direct dependence of the output electrical energy *U* on the out-of-plane displacement w_0 which is equal to *w* of the whole sandwich plate in the view of negligible *z*-displacement, which is justified for slender plates.

To find the out-of-plane displacement for the middle plane of the PZT-composite, the force generated by the SMA composite must be found (*N(x,y,t)*). Knowing the force generated by the SMA composite it will be possible to find the displacement of the active PZT-composite elements and the energy output according to (4).

Therefore, the problem is now reduced to finding the displacement of a PZT-element, which is defined by the following governing equation for a composite plate for the general case of any boundary conditions [31]

$$D_{11}\frac{\partial^4 w}{\partial x^4}+2(D_{12}+2D_{66})\frac{\partial^4 w}{\partial x^2\partial y^2}+D_{22}\frac{\partial^4 w}{\partial y^4}-N(x,y,t)\frac{\partial^2 w}{\partial x^2}=p(x,y)-2\rho\varepsilon h\frac{\partial w}{\partial t}-\rho h\frac{\partial^2 w}{\partial t^2} \tag{5}$$

where $\rho=\sum_{i=1}^{3}\frac{\rho_i h_i}{h}$, h_i is the thickness of the *i*-th lamina, and *h* is the thickness of the whole plate. Since we are considering the case when the force is generated by the SMA composite, the activation process can be treated as if we were using the Active Strain Energy Tuning (ASET) method [13,14]. The optimal location and orientation of wires within the SMA composite is discussed in detail in [13,14].

Investigating the case of ASET, we assume that the plate with PZT patches (PZT-composite) is restrained and under initial tension due to the spring loading *p(x,y)*, and experiences the force generated by SMA composite during the activation. It should also be pointed out that we are considering an environment with dynamic thermal changes, thus the force created by the SMA-composite is time dependent *N=N(x,y,t)*.

It should be noted that the plate's stiffness is characterized by parameters D_{11}, D_{22}, D_{12} and D_{66}. These bending stiffnesses can be defined for a laminated composite plate, as in [32]

$$D_{jk}=\frac{2}{3}\left[B_{jk}^{N/2}h_{N/2}^3+\sum_{i=1}^{N/2-1}B_{jk}^{i}\left(h_i^3-h_{i+1}^3\right)\right] \tag{6}$$

where *N* is the number of layers, and B_{jk}^{i} denotes the elastic coefficients for the *i*-th lamina. For the sandwich plate considered in Fig. 2:

$$D_{jk}=\frac{2}{3}\left[B_{jk}^{0}\delta_0^3+B_{jk}\left(\delta^3-\delta_0^3\right)\right] \tag{7}$$

The fact that the PZT-composite's top and bottom layers have the same dimensions and properties has also been taken into account, i.e. $B_{jk}^{1}=B_{jk}^{2}=B_{jk}$, whilst the middle ply has different properties, B_{jk}^{0}. It should be noted that $2\delta_0$, $\delta-\delta_0$, $\delta-\delta_0$ are the thicknesses of the middle, top and bottom layers, respectively; *i* is the index of the ply such that *i* = 0 for the middle layer, and *i* = 1 and *i* = 2 are for the top and bottom layers respectively. It should be noted that the middle layer of the PZT-composite possesses only elastic properties and has no PZT patches, hence:

$$B_{11}^{0}=\frac{E_{11}^{0}}{1-\nu_{12}^{0}\nu_{21}^{0}},\ B_{22}^{0}=\frac{E_{22}^{0}}{1-\nu_{12}^{0}\nu_{21}^{0}},\ B_{12}^{0}=\frac{\nu_{12}^{0}E_{12}^{0}}{1-\nu_{12}^{0}\nu_{21}^{0}},\ B_{66}^{0}=G_{12}^{0} \tag{8}$$

.

And for the top and bottom active layers (with PZT patches) according to [32]:

$$B_{11}=\frac{E_{11}}{1-\nu_{12}\nu_{21}},\ B_{22}=\frac{E_{22}}{1-\nu_{12}\nu_{21}},\ B_{12}=\frac{\nu_{12}E_{12}}{1-\nu_{12}\nu_{21}},\ B_{66}=G_{12} \tag{9}$$

,

where

$$\begin{aligned}&E_{11}=E_fV+E_m(1-V),\ E_{22}=E_m\frac{E_f+E_m+(E_f-E_m)V}{E_f+E_m-(E_f-E_m)V},\\&G_{12}=G_m\frac{G_f+G_m+(G_f-G_m)V}{G_f+G_m-(G_f-G_m)V},\ \nu_{12}=\nu_fV+\nu_m(1-V),\\&\hat{\rho}=\rho_fV+\rho_m(1-V),\end{aligned} \tag{10}$$

and V is the relative volume fraction of the PZT in the i-th lamina, f denotes the PZT material/fibre, and m represents the matrix or host material.

The density of the whole plate in this case is given by

$$\rho = \sum_{i=1}^{3} \frac{\rho_i h_i}{h} = \frac{2}{h}\left[\hat{\rho}(\delta - \delta_0) + \rho_0 \delta_0\right] \tag{11}$$

where $\hat{\rho}$ is the density of the PZT-composite layers defined in (9), and ρ_0 is the density of the elastic middle layer without the PZT fibre.

The deflection of a simply supported plate can be expressed as [32]

$$w(x, y, t) = f(t) \sin\left(\frac{\pi x}{a}\right) \sin\left(\frac{\pi y}{b}\right) \tag{12}$$

and the loading $p(x,y)$

$$p(x, y) = p \sin\left(\frac{\pi x}{a}\right) \sin\left(\frac{\pi y}{b}\right). \tag{13}$$

Therefore, introducing the following

$$\widetilde{D} = \pi^4 \left(\frac{D_{11}}{a^4} + 2\frac{D_{12} + 2D_{66}}{a^2 b^2} + \frac{D_{22}}{b^4} \right), \; \bar{N}(t) = \left(\frac{\pi}{a}\right)^2 N(t) \tag{14}$$

where $N(t) = A\cos\Omega t$ and after applying Eq. (3), Eq. (5) can be expressed as

$$\lambda^2 f''(t) + 2\bar{\varepsilon} f'(t) + \bar{\bar{D}}(t) f(t) = \tilde{q}(t) \tag{15}$$

where $\lambda^2 = \frac{h}{a}$; $\bar{\varepsilon} = \frac{h}{a}\varepsilon$; $\bar{\bar{D}}(t) = \frac{1}{\rho a}\left[\widetilde{D} + \bar{N}(t)\right]$, and assumed $\tilde{q}(t) = \tilde{q} = \frac{p}{\rho a}$.

Equation (15) is a nonhomogeneous differential equation with variable coefficients, and can be solved analytically applying an approximate analytical technique. To find the complementary function for the homogeneous equation of Eq. (15) the hybrid Wentzel–Kramers–Brillouin–Galerkin (or WKB–Galerkin) method [32,33] has been applied following [32]. In this case the solution based on two stages of the hybrid WKB–Galerkin can be expressed as

$$f(t) = e^{-\delta_{02}\int_{\bar{a}}^{t} \bar{f}_0(t)dt} \left[(s_1 + c_1) \sin\left(\delta_{01} \int_{\bar{a}}^{t} \bar{f}_0(t)dt \right) + (s_2 + c_2) \cos\left(\delta_{01} \int_{\bar{a}}^{t} \bar{f}_0(t)dt \right) \right] \tag{16}$$

where $\bar{f}_0 = \left[2 \int \frac{e^{2\int \frac{\bar{\bar{D}}(t)}{\bar{\varepsilon}} dt}}{\bar{\varepsilon}} dt \right]^{-1/2} e^{\int \frac{\bar{\bar{D}}(t)}{\bar{\varepsilon}} dt}$, $\begin{cases} \delta_{01} = \pm \frac{\sqrt{4BW - A^2}}{2B} \\ \delta_{02} = \pm \frac{A}{2B} \end{cases}$ and

$$s_1 = \int \frac{\tilde{q}(t) e^{\delta_{02}\int_{\bar{a}}^{t} \bar{f}_0(t)dt} \cos\left(\delta_{01} \int_{\bar{a}}^{t} \bar{f}_0(t)dt \right)}{\lambda^2 \delta_{01} \frac{d}{dt}\left(\int_{\bar{a}}^{t} \bar{f}_0(t)dt \right)} dt \qquad s_1 = -\int \frac{\tilde{q}(t) e^{\delta_{02}\int_{\bar{a}}^{t} \bar{f}_0(t)dt} \sin\left(\delta_{01} \int_{\bar{a}}^{t} \bar{f}_0(t)dt \right)}{\lambda^2 \delta_{01} \frac{d}{dt}\left(\int_{\bar{a}}^{t} \bar{f}_0(t)dt \right)} dt ,$$

$A = \int_a^b \left[-\lambda^2 \dot{\bar{f}}_0 \bar{f}_0 - 2\bar{\varepsilon}\overline{\bar{f}_0^2} \right] dt$, $B = \int_a^b \lambda^2 \overline{\bar{f}_0^3} dt$, and $W = \int_a^b \bar{\bar{D}}(t) \bar{f}_0 dt$.

2.3 Finite element model

Figure 3 shows a composite plate with multiple layers containing embedded PZT patches. The plate being modelled is of length 0.1 m, width 0.05 m, and thickness 0.0005 m, it worth noting however that these dimensions are arbitrary. There are 4 layers total, arranged symmetrically about the central plane, each with a ply thickness of 0.000125m. The two outer layers contain the PZT (dotted blue) patches embedded in the CFRP (solid orange) host material, with two middle layers of CFRP host material, as shown in Fig. 3. For the analytical models, the two outer layers are modelled as a mix of the PZT and CFRP at a volume fraction of 0.72 for the PZT. The FE model has four PZT patches that are all of length 0.045 m, and width 0.04 m, and are spaced 0.0025 m away from any edge. The CFRP host material is a carbon-fibre/epoxy 0/90 weave and assumed to be isotropic. In the parts of the device not covered by the patches, all 4 plies are made of CFRP, again shown in Fig. 3. Table 1 shows these dimensions along with the material properties.

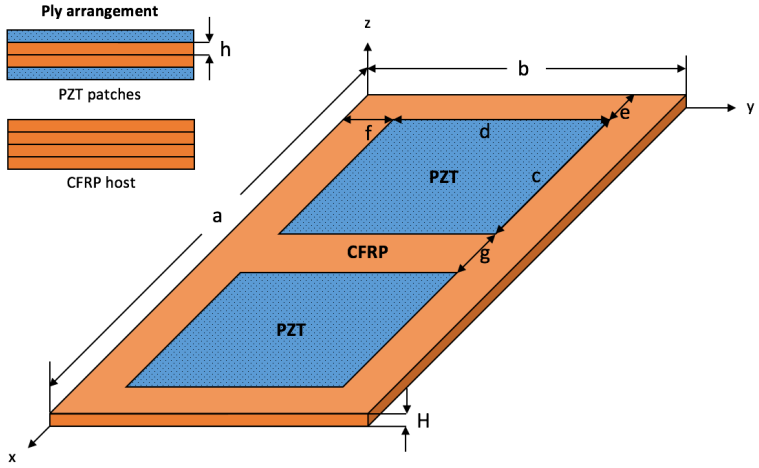

Figure 3. A schematic showing the dimensions and ply arrangement for the multilayered composite plate with embedded PZT patches

A convergence study was carried out using the minimum and maximum *z*-displacement in order to check the required mesh size. It was found that the displacement results were not sensitive to mesh size and so an element size of 0.00125 m was chosen to limit computing time while still producing good accuracy. The final mesh is shown in Fig. 4.

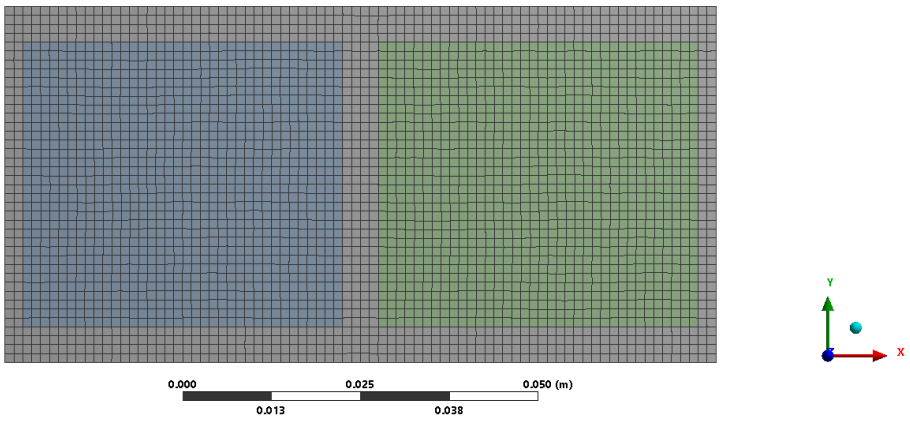

Figure 4. Image showing the final mesh used in the finite element model

The plate was assumed to have only the z-displacement fixed along all of the edges, except the edge coincident to the y-axis, which was simply supported. The force was applied along the opposite edge to the simply supported edge and was of the form $F = -150 \cdot cos(6206t)$ N. This is based on the force of 19.62 N produced by a typical commercially available SMA wire of diameter $3.81 \cdot 10^{-4}$ m, made of NiTi. A surface distributed loading of 0.01 N was applied in the negative z-direction. A numerical damping of 0.0000322 was chosen to match the analytical model. An initial displacement of 0.0001 m was applied.

Table 1. List of dimensions for the HEHD as well as material properties for both materials

Material	**Parameter**	**Value**	**Units**
CFRP	Length a	0.1	m
	Width b	0.05	m
	Overall thickness H	0.0005	m
	Young's Modulus	$70.0 \cdot 10^{9}$	N/m^2
	Poisson's Ratio	0.10	---
	Density	1600	kg/m^3
PZT	Patch length c	0.045	m
	Patch width d	0.04	m
	Patch thickness h	0.000125	m
	Spacing e	0.0025	m
	Spacing f	0.005	m
	Separation g	0.005	m
	Young's Modulus	$67.0 \cdot 10^{9}$	N/m^2
	Poisson's Ratio	0.31	---
	Density	7800	kg/m^3
	Piezoelectric charge constant d_{33}	$450 \cdot 10^{-12}$	C/N
	Piezoelectric charge constant d_{31}	$-175 \cdot 10^{-12}$	C/N
	Piezoelectric voltage constant g_{33}	0.027	Vm/N
	Piezoelectric voltage constant g_{31}	-0.011	Vm/N

3 RESULTS

One finding of the models was that the system behaves parametrically. This can be seen from Fig. 5, which shows the dynamic response at a driving frequency of 6206 rad/s. Figure 5a shows the frequency content of the response which reveals parametric behaviour. This is further shown by Fig. 5b, in which we can see the response becomes unstable and grows. The analytical results shown in Fig. 6 display parametric behaviour, but they are stable.

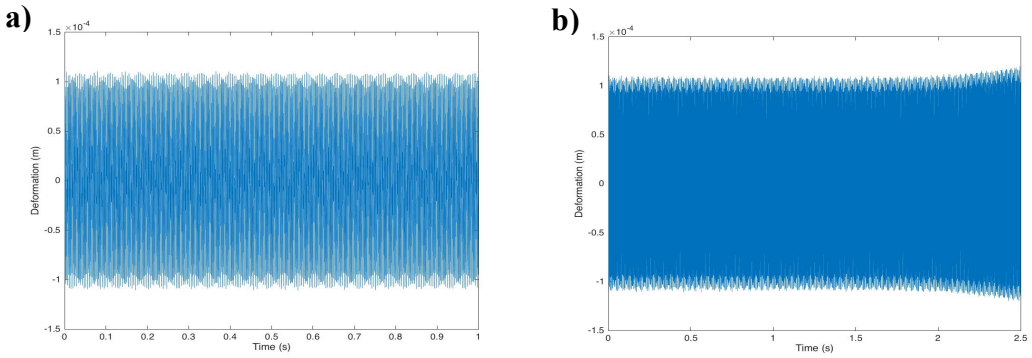

Figure 5. Parametric vibrational response for the finite element model of the HEHD with an excitation frequency of 989 Hz over a) 1 second and b) 2.5 second intervals

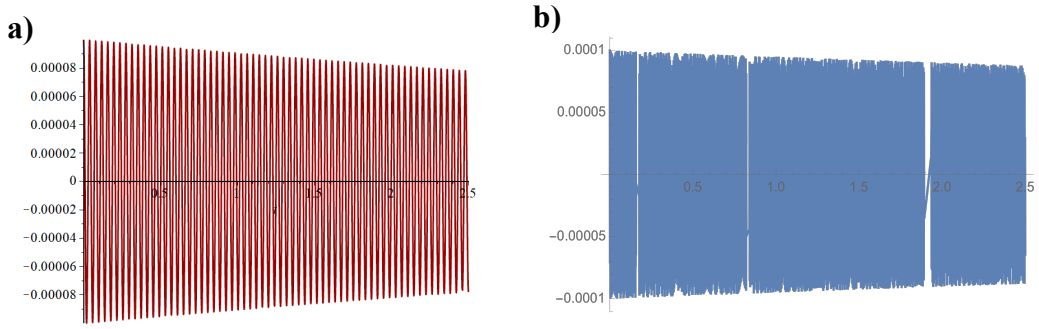

Figure 6. Analytical (a) and numerical (b) solution results over a 2.5 second interval

Applying the analytical solution represented by the closed function in Eq. (16) to the numerical values described in Section 2.3 for the FE model, it was possible to obtain the results shown in Fig. 6a. It should be noted that a major benefit of the analytical model is that it is obtained as a closed function, which allows us to see the distribution of vibration over a longer period without significant computational time and memory requirements. We also present a numerical solution of Eq. (16) for verification purposes, obtained using the commercial software Mathematica.

From Fig. 6a, in comparison with Fig. 5, it can be seen that WKB-Galerkin method analytical solution is very good in predicting the behaviour of the system, corresponding to the frequency of the the force applied; though due to the complex integration in Eq. (16) some *cos* and *sin* functions were simplified with series expansions, which obviously results in lower precision in terms of the frequency of the output vibration. The frequency of the vibration obtained using numerical solution and FE model demostrate very close similarity.

The average power of **73.5 mW** has been calculated for the FE model and is based on the x and y normal stress output for a single patch over using Eq. (4) and averaging over the time period of 1 second. The total energy converted in the entire harvester would be **588 mW** as there are 8 patches in the device. Nonetheless, this is an estimate of the energy produced in the PZT patches and not an estimate of how much would be harvested by attached circuitry.

4 DISCUSSION

The FE and analytical models both display a parametric vibrational response. However, in the FE model the response become unstable after 2 seconds, while the response from the analytical model decays gradually over time. By using a high input frequency, it can be shown that the system behaves parametrically and it gives confidence in the ability of both models to predict complex dynamic behaviour beyond simple free or forced vibration. The output displacement is the same for both models and comes from the initial conditions. Whether or not the response is stable or unstable is highly sensitive to the dynamic properties of the system. The difference in the stability of the response of the two models is almost certainly due to the difference in how the PZT is included in the model. By concentrating the PZT into patches, the natural frequencies and mode shapes of the device will change.

The electrical energy predicted by the FE model for a single cycle (assuming 494 Hz output frequency) is **1.19 mJ**, which is comparable to a snap-through energy harvester which has an energy output of **20.4 mJ - 33.7 mJ** [29] per cycle. A snap-through energy harvester will tend to have a higher energy per cycle, but it may not perform as well at higher frequencies. The overall volume of the HEHD is 5 cm^3, excluding the SMA, making its power density **118 mW/cm^3**, which is higher than the values of **800 μW/cm^3** estimated for other vibrational generators in the kHz range [34]. It is worth noting that the displacement predicted for the other vibrational generator is significantly less, being on the nanometer scale instead of the micrometer scale. The increased displacement found with this model is likely due to the parametric behaviour exhibited.

While both of these models are examining the same behaviour, there are limitations and benefits for each approach. The FE model could be used for static modelling and by displaying the stress distribution, the effect of patch configuration on the stress concentrations can be investigated. The FE model becomes less useful for high frequency simulations as small step sizes are required to accurately capture the vibrational response without aliasing. This limits the duration over which high frequency behaviour can be studied, as the computational time becomes prohibitive. The analytical models are therefore better suited for studying high frequency behaviour over a long period of time. The analytical model gives functions for the displacement and strain, whereas the FE model only gives these results as points. The benefit of using the analytical model in this case is that these functions for the results can be further manipulated.

5 CONCLUSION

Both the FE and analytical models show that the device behaves parametrically for the same input frequency. The results verify both of the approaches and yield an interesting insight into the dynamic behaviour of the device. The device has been shown to have energy and power outputs comparable to existing devices which are similar in design, this gives further confidence in the model results as well as the harvester design. The shape memory effect has not been directly incorporated in this paper, however the forcing function for a given SMA can be fed into either model. Combining models for the piezoelectric and SMA elements in the device could form the basis for future work. The merits and limitations of the two approaches have been discussed, providing a recommendation for where each is most applicable.

6 REFERENCES

1. Shaikh, F.K., Zeadally, S. Energy harvesting in wireless sensor networks: A comprehensive review. *Renewable and Sustainable Energy Reviews*, 2016; **55**:1041-1054.
2. Dagdeviren, C., Yang, B.D., Su, Y., et al. Conformal piezoelectric energy harvesting and storage from motions of the heart, lung, and diaphragm. *Proceedings of the National Academy of Sciences of the United States of America*, 2014; **111**(**5**):1927-1932.
3. Roundy, S., Wright, P.K., Rabaey, J. A study of low level vibrations as a power source for wireless sensor nodes. *Computer Communications*, 2003; **26**(**11**):1131-1144.
4. Sodano, H.A. Generation and Storage of Electricity from Power Harvesting Devices. *Journal of Intelligent Material Systems and Structures*, 2005; **16**(**1**):67-75.
5. Umeda, M., Nakamura, K., Ueha, S. Energy Storage Characteristics of a Piezo- Generator using Impact Induced Vibration. *Japanese Journal of Applied Physics*, 1997; **36**(**5B**):3146-3151.
6. Horowitz, S.B., Sheplak, M., Cattafesta, L.N., Nishida, T. A MEMS acoustic energy harvester. *Journal of Micromechanics and Microengineering*, 2006; **16**(**9**):S174-S181.
7. Cuadras, A., Gasulla, M., Ferrari, V. Thermal energy harvesting through pyroelectricity. *Sensors and Actuators, A: Physical*, 2010; **158**(**1**):132-139.
8. Sodano, H.A., Park, G., Inman, D.J. An investigation into the performance of macro-fiber composites for sensing and structural vibration applications. *Mechanical Systems and Signal Processing*, 2004; **18**(**3**):683-697.
9. Baker, J. Alternative Geometries for Increasing Power Density in Vibration Energy Scavenging. *3rd International Energy Conversion Engineering Conference 15 - 18 August 2005, San Francisco, California*, 2005;(**August**):1-12.
10. Sodano, H.A., Inman, D.J., Park, G. Comparison of piezoelectric energy harvesting devices for recharging batteries. *Journal of Intelligent Material Systems and Structures*, 2005; **16**(**10**):799-807.
11. Kymissis, J., Kendall, C., Paradiso, J., Gershenfeld, N. Parasitic power harvesting in shoes. *Digest of Papers Second International Symposium on Wearable Computers (Cat No98EX215)*, 1998:2-9.
12. Ramesy, M.J., Clark, W.W. Piezoelectric energy harvesting for bio MEMS applications. In: *SPIE's 8th Annual Smart Materials and Sturctures Conference, Vol. 4332-2001*. Newport Beach, CA; 2001:429-438.
13. Żak, A.J., Cartmell, M.P., Ostachowicz, W.M. A sensitivity analysis of the dynamic performance of a composite plate with shape memory alloy wires. *Composite Structures*, 2003; **60**(**2**):145-157.
14. Zak, A.J., Cartmell, M.P., Ostachowicz, W. Dynamics of Multilayered Composite Plates With Shape Memory Alloy Wires. *Journal of Applied Mechanics*, 2003; **70**(**3**):313.
15. Ostachowicz, W., Cartmell, M., Zak, A. Statics and dynamics of composite structures with embedded shape memory alloys. *Advanced course on structural …*, 2001.
16. Zak, A.J., Cartmell, M.P. Control of vibrations by SMA components. *2nd International Conference on Advanced Engineering Design*, 2001.
17. Zak, A.J., Cartmell, M.P., Ostachowicz, W.M., Wiercigroch, M. One-dimensional shape memory alloy models for use with reinforced composite structures. *Smart Materials and Structures*, 2003; **12**(**3**):338.
18. Brinson, L.C., Lammering, R. Finite element analysis of the behavior of shape memory alloys and their applications. *International Journal of Solids and Structures*, 1993; **30**(**23**):3261-3280.
19. Brinson, L.C. One-Dimensional Constitutive Behavior of Shape Memory Alloys: Thermomechanical Derivation With Non-Constant Material Functions and Redefined Martensite Internal Variable. *Journal of intelligent material systems and structures*, 1993; **4**(**2**):229-242.
20. Thrasher, M.A., Shahin, A.R., Mecklts, P.H., Jones, J.D. Efficiency analysis of shape memory alloy actuators. 1994; **226**.

21. Liu, Y. The work production of shape memory alloy. *Smart Materials and Structures*, 2004; **13**(**3**):552-561.
22. Otsuka, K., Ren, X. Physical metallurgy of Ti-Ni-based shape memory alloys. *Progress in Materials Science*, 2005; **50**(**5**):511-678.
23. Paradiso, J.A., Starner, T. Energy scavenging for mobile and wireless electronics. *IEEE Pervasive Computing*, 2005; **4**(**1**):18-27.
24. Reddy, A.R., Umapathy, M., Ezhilarasi, D., Uma, G. Piezoelectric Energy Harvester With Shape Memory Alloy Actuator Using Solar Energy. 2015; **6**(**4**):1409-1415.
25. Gusarov, B., Gimeno, L., Gusarova, E., Viala, B., Boisseau, S., Cugat, O. Flexible composite thermal energy harvester using piezoelctric PVDF polymer and shape memory alloy. *IEEE Solid-State Sensors, Actuators and Microsystems (TRANSDUCERS)*, 2015:722-725.
26. Namli, O.C., Taya, M. Design of Piezo-SMA Composite for Thermal Energy Harvester Under Fluctuating Temperature. *Journal of Applied Mechanics*, 2011; **78**(**3**):031001.
27. Taylor, N.A.S., Tipton, M.J., Kenny, G.P. Considerations for the measurement of core, skin and mean body temperatures. *Journal of Thermal Biology*, 2014; **46**:72-101.
28. Wakamatsu, M., Nei, H., Hashiguchi, K. Attenuation of Temperature Fluctuations in Thermal Striping. *Journal of Nuclear Science and Technology*, 1995; **32**(**8**):752-762.
29. Betts, D.N., Kim, H.A., Bowen, C.R., Inman, D.J. Optimal configurations of bistable piezo-composites for energy harvesting. *Applied Physics Letters*, 2012; **100**(**11**):2010-2014.
30. Kollár, L.P., Springer, G.S. *Mechanics of Composite Structures*. Cambridge University Press; 2003.
31. Zak, A.J., Cartmell, M.P. Analytical modeling of shape memory alloys and flat multi-layered composite beams and plates with shape memory alloy wires. *1st Report, Grant GR/N06267/01*, 2000.
32. Ganilova, O.A., Cartmell, M.P. An analytical model for the vibration of a composite plate containing an embedded periodic shape memory alloy structure. *Composite Structures*, 2010; **92**(**1**):39-47.
33. Gristchak, V.Z., Ganilova, O.A. A hybrid WKB-Galerkin method applied to a piezoelectric sandwich plate vibration problem considering shear force effects. *Journal of Sound and Vibration*, 2008; **317**(**1-2**):366-377.
34. Mitcheson, P.D., Green, T.C., Yeatman, E.M., Holmes, A.S. Architectures for vibration-driven micropower generators. *Journal of Microelectromechanical Systems*, 2004; **13**(**3**):429-440.